RESEARCH ARTICLE

NANO · MICRO small
www.small-journal.com

Scanning Electrochemical Microscopy Meets Optical Microscopy: Probing the Local Paths of Charge Transfer Operando in Booster-Microparticles for Flow Batteries

Mahdi Moghaddam, Louis Godeffroy, Jerzy J. Jasielec, Nikolaos Kostopoulos, Jean-Marc Noël, Jean-Yves Piquemal, Jean-François Lemineur, Pekka Peljo, and Frédéric Kanoufi**

Understanding the oxidation/reduction dynamics of secondary microparticles formed from agglomerated nanoscale primary particles is crucial for advancing electrochemical energy storage technologies. In this study, the behavior of individual copper hexacyanoferrate (CuHCF) microparticles is explored at both global and local scales combining scanning electrochemical microscopy (SECM), for electrochemical interrogation of a single, but global-scale microparticle, and optical microscopy monitoring to obtain a higher resolution dynamic image of the local electrochemistry within the same particle. Chronoamperometric experiments unveil a multistep oxidation/reduction process with varying dynamics. On the one hand, the global SECM analysis enables quantifying the charge transfer as well as its dynamics at the single microparticle level during the oxidation/reduction cycles by a redox mediator in solution. These conditions allow mimicking the charge storage processes in these particles when they are used as solid boosters in redox flow batteries. On the other hand, optical imaging with sub-particle resolution allows the mapping of local conversion rates and state-of-charge within individual CuHCF particles. These maps reveal that regions of different material loadings exhibit varying charge storage capacities and conversion rates. The findings highlight the significance of porous nanostructures and provide valuable insights for designing more efficient energy storage materials.

1. Introduction

The rise of renewable energy sources and the concurrent decrease in fossil fuel usage necessitate reliable large-scale energy storage solutions. Among them, flow batteries (FBs) have emerged as promising candidates for large-scale energy storage thanks to their unique capability to decouple energy and power.[1,2] Nonetheless, their limited energy density remains a challenge to overcome.[3]

An innovative solution to enhance the energy density of FBs lies in the redox targeting[4–7] or solid booster (SB) concept.[8–10] Here, redox-active solid particles are added to the tank, serving as the main energy storage medium. The dissolved redox couples now principally function as mediators, delivering charge from the cell to these confined solid particles. As these solids inherently possess a higher charge storage density than the redox electrolyte, this approach enables an overall augmentation in charge storage density, thereby elevating the energy density beyond the limit set by the solubility of the dissolved redox couples.[8,10]

This strategy introduces a new interface between the solid particles and the electrolyte as well as a new charge transfer reaction. The intricacies of this reaction, a coupled electron-ion transfer where the dissolved cation in the electrolyte intercalates into the solid particle, mandate thorough thermodynamic and kinetic studies, within recent theoretical frameworks,[11] for the development and optimization of the solid-boosted configuration. To optimize flow batteries

M. Moghaddam, J. J. Jasielec, P. Peljo
Research Group of Battery Materials and Technologies
Department of Mechanical and Materials Engineering
Faculty of Technology
University of Turku
Turun Yliopisto 20014, Finland
E-mail: pekka.peljo@utu.fi
The ORCID identification number(s) for the author(s) of this article can be found under https://doi.org/10.1002/smll.202309607

DOI: 10.1002/smll.202309607

L. Godeffroy, N. Kostopoulos, J.-M. Noël, J.-Y. Piquemal, J.-F. Lemineur, F. Kanoufi
Université Paris Cité
CNRS
ITODYS
Paris F-75013, France
E-mail: frederic.kanoufi@u-paris.fr
J. J. Jasielec
Department of Physical Chemistry and Modelling
Faculty of Materials Science and Ceramics
AGH University of Science and Technology
Al. Mickiewicza 30, Kraków 30-059, Poland

employing solid boosters, measurement techniques able to obtain information about the limiting processes of charge transfer between solid and liquid species are required. For example, the charge transfer can be limited by kinetics, transport of intercalated cation within the solid, or transport of mediator close to the solid. Optimizing and designing a functioning system will require an understanding of the limiting steps. If charge transfer is the limiting process, suitable catalysts as well as methods to maximize the surface area should be explored, while slow transport in the solid would require decreasing the diffusion length by decreasing size. Transport of mediator could be improved by increased convection, etc.

This work proposes an operando high-resolution imaging methodology of such configuration in the case of the oxidation/reduction of a single micrometric secondary particle of copper hexacyanoferrate (CuHCF), a Prussian blue analog (PBA).[12,13] In these materials, many nanometer-scale primary particles can agglomerate to form micrometer-scale porous secondary particles. Our recent research has focused on the thermodynamics of such solid-boosted flow batteries (SB-FBs) and their techno–economic design.[14] Yet, the kinetics of such systems have been somewhat neglected, likely due to their inherent complexity.[15–19] Unraveling the kinetics of SB-FBs, specifically the charge transfer kinetics between the solid and the electrolyte in the tank, is indeed a challenging task given the intricate nature of the reaction combining interfacial chemistry and mass transfer both in the solid and in the electrolyte, which calls for operando exploration.[20] Particularly, achieving the fast conversion and mass transfer rates required for high-power density SB-FBs calls for porous solid phases, such as secondary particles formed from agglomerates of small primary particles, thereby resulting in mixed surface (capacitor-like) and bulk (battery-like) conversion behaviors [21–23] showing up at different micro- to nanoscale observation lengths.

Scanning electrochemical microscopy (SECM) provides a robust platform to study these complex systems. Indeed, the local probe of the SECM, an ultramicroelectrode (UME), can be used to trigger and probe the conversion of such materials at the scale of the UME size, as in the so-called "surface interrogation" mode (SI-SECM).[17,19,24,25] This approach is particularly useful in the context of SB-FBs as it allows the charge storage/extraction in the redox solid to be tracked operando.[20,26–31]

While SECM, with the classical 12.5 µm size UME, allows interrogating the charge storage/extraction at the single microparticle level, tracking these processes at the single-nanocrystal level is challenging as it would require a UME of comparable size to these nanocrystals. Therefore, alternative single-particle electrochemical techniques [26–32] need to be explored to deepen our understanding of the conversion mechanisms at the nanoscale. Optical microscopy techniques, for instance, provide exceptional spatial, temporal, and throughput resolution, granting unique insights into the electrochemistry of materials for electrochemical energy storage at both macro-,[23] micro-,[33–37] and nanoscale.[21,38–43] For instance, Wang et al. evaluated the K^+ diffusion dynamics within single PB nanoparticles (NPs).[38–40] Meanwhile, Merryweather et al.[33–35] and Pandya et al.[37] showed how optical microscopy allows imaging operando the Li^+ insertion front lines within single micrometric battery particles during their oxidation/reduction. However, a gap is left unfilled regarding the understanding of charge storage within secondary particles. Indeed, this requires considering, not only the microstructure of the particle but also its individual building blocks (NPs) and the intrinsic porosity of such assembly. It further allows, at least with macroscale measurement, to explore the full diversity of charge storage behaviors, from capacitor to battery-like.[23] This work also helps to develop generalized models to predict the effects of properties of secondary particles such as porosity etc. on the performance of the system.

To explore such complex conversion/transport processes, we propose combining SECM and optical microscopy. Different optical imaging techniques, including those with spectroscopic potentialities, have already been combined with scanning electrochemical probe microscopies, using UMEs [17,25,44–50] or nanopipettes [30,31,51–53] as local electrochemical probes. This approach leverages the UME of the SECM to trigger and probe the electrochemical oxidation/reduction of a single SB particle, while simultaneously monitoring its conversion at a sub-particle resolution and operando using optical microscopy. In this novel approach, depicted in **Figure 1**, the UME serves as a mirror, allowing to investigation of local changes in absorption and hence to probe the coupled electron transfer and K^+ (de)intercalation from/into single micrometric porous CuHCF particles.[12,13] This innovative strategy, supported by finite elements simulations of the transport/reaction in porous media, unveils the significant role of surface versus bulk conversion dynamics and identifies preferential porous pathways for the redox electrolyte via nanoscale operando optical imaging. Doing so, paves the way for a better understanding and performance optimization of SB-FBs but also for other batteries utilizing secondary particles of active material.

2. Results and Discussion

2.1. Probing the Oxidation/Reduction of Individual CuHCF Microparticles by Opto–Electrochemistry

2.1.1. Principle

CuHCF particles have emerged as promising solid boosters for the positive side of SB-FBs,[8] when combined with N,N,N-2,2,6,6-heptamethyl piperidinyl oxy-4-ammonium chloride (TEMPTMA) [1] as the redox mediator. Their appeal lies in their closely aligned redox potentials, $E°_{CuHCF} = +0.97$ V versus SHE and $E°_{TEMPTMA} = +0.91$ V versus SHE, resulting in optimal utilization of the solid's charge storage capacity.[14] This way, the solid particle can be both charged and discharged with the same mediator. In addition, the redox mediator should exhibit low optical absorption for minimal interference with the CuHCF's absorption spectrum. Figure S5 (Supporting Information) shows that the TEMPTMA redox mediator has minimal absorption variations in all color channels. For these two reasons, CuHCF-TEMPTMA system was selected as a model system for this investigation.

We investigate the oxidation/reduction processes of individual CuHCF secondary particles using a hybrid approach that combines local electrochemical triggering and interrogation by SECM with concurrent operando optical imaging. Figure 1

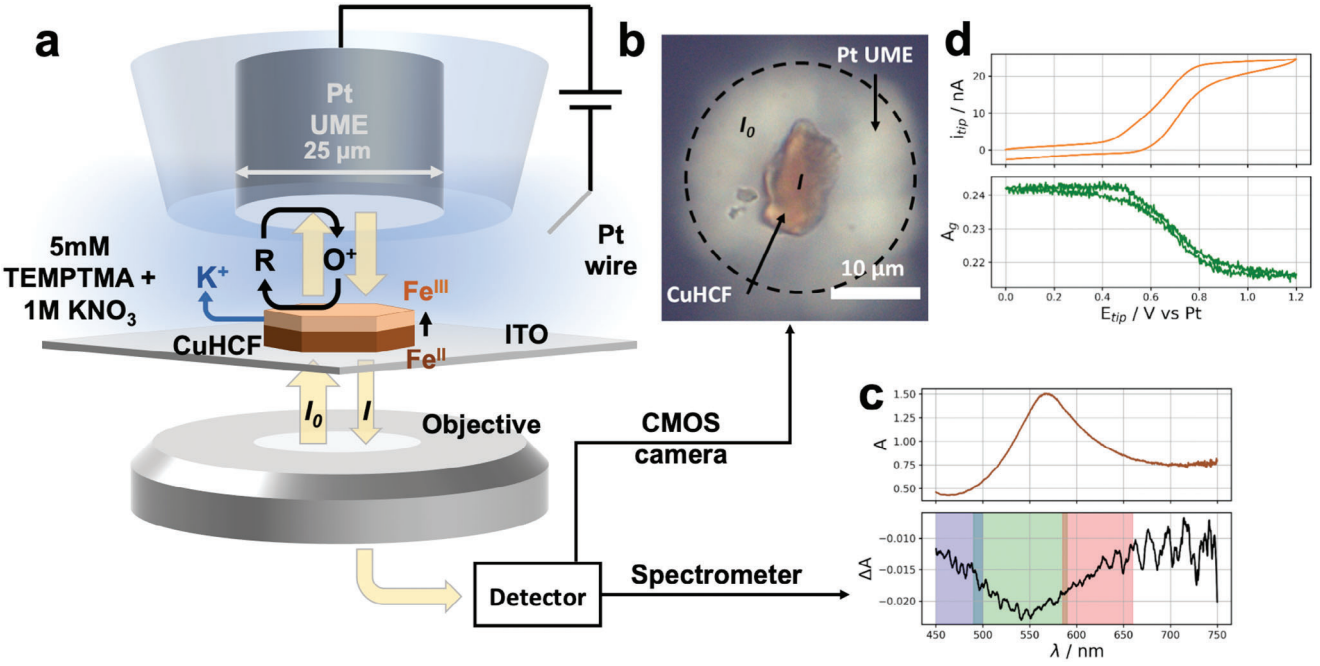

Figure 1. a) Principle of the optical monitoring of the oxidation then reduction of a single CuHCF particle triggered by the electrogeneration of the redox mediator (O^+) at the SECM's UME (25 µm-diameter Pt disk) held above it. The yellow arrows illustrate the light path enabling local absorbance measurements, utilizing the UME as a mirror. b) Raw color optical image displaying the pristine CuHCF particle alongside the mirror-like UME. c) Absorbance spectrum of the single particle and its variation, ΔA, upon oxidation. Overlaid are the spectral ranges to which each color channel of the camera is sensitive. d) Transient evolution of the tip current (top) and absorbance, A_g (bottom), measured from the green channel of the camera, during a movie of the particle acquired at 20 frames s^{-1} (fps), and averaged over ≈2.75 × 2.75 μm^2 region of interest of the particle, during cyclic voltammetry conducted in a solution containing 5 mM TEMPTMA (R) + 1 M KNO_3 at the Pt UME held at a distance of 10 µm above the ITO surface (≈7 µm above the top of the 3 µm thick CuHCF particle, see 3D SEM image in Figures S2-3, Section S2, Supporting Information).

illustrates the operational concept of this integrated SECM-optical microscopy setup.

The secondary particles of CuHCF used in this study are micrometric particles obtained by wet chemical synthesis described in supporting information, SI, Section S1 (Supporting Information). The resulting microparticles were characterized by X-ray diffraction (Figure S1, Supporting Information) and inductively coupled plasma–optical emission spectroscopy (ICP, see Section S1.2, Supporting Information). The X-ray diffractogram is consistent with the reported XRD patterns for analogously synthesized CuHCF crystals.[54] The generic composition of CuHCF can be described as a mixture of its reduced form, $K_2Cu_3[Fe^{II}(CN)_6]_2$, and of its oxidized form, $Cu_3[Fe^{III}(CN)_6]_2$. Denoting x the content of the reduced form, the general expression of CuHCF writes $K_{2x}Cu_3[Fe^{II}{}_xFe^{III}{}_{1-x}(CN)_6]_2$ or equivalently $K_{2x}Cu_3[Fe(CN)_6]_2$,[54,55] where $x = 1$ for fully reduced CuHCF form and $x = 0$ for fully oxidized CuHCF form. ICP analysis of the elements K, Cu, and Fe in the synthesized batch yields a composition of $K_{0.97}Cu_3Fe_{1.59}$ in agreement with a CuHCF structure and with $x = 0.61$. The partially reduced form of the CuHCF material to 61% is also consistent with the observed XRD pattern.[54]

Structural characterization of these CuHCF secondary particles was carried out by scanning electron microscopy (SEM) and scanning transmission electron microscopy (STEM). The SEM and STEM images provided in Figures S2-1 and S2-2, Section S2 (Supporting Information), show that these secondary particles are formed from agglomerated primary particles (30–100 nm). The size of the primary particles is in agreement with earlier reports.[13]

The as-synthetized CuHCF secondary particles are then drop-casted from a dilute water suspension onto an optically transparent indium tin oxide (ITO) substrate. This substrate, decorated with CuHCF microparticles, is positioned on the stage of an inverted optical microscope and illuminated from the backside (bottom) using unpolarized white light through a 63×, 1.4 numerical aperture, oil-immersion objective (additional details are available in Section S3, Supporting Information). The optical microscope serves a dual purpose: 1) targeting [30] individual particles to facilitate the precise positioning of the tip of the SECM 25 µm-diameter Pt disk UME only a few micrometers, ≈7 µm (10 µm above the substrate), above the ≈3 µm thick chosen particle (from 3D SEM image in Section S2, Supporting Information), and 2) imaging them at the nanoscale during their conversion.

The procedure for targeting and enabling the precise interrogation of an individual particle is described schematically in **Figure 2**. In brief, the UME is roughly approached to the support (down to ca. several tens of µm). Once it is within the field of view of the microscope objective the UME surface, detected as a bright disk (Figure 2a), is then approached to ≈10 µm from the substrate (evaluated from the focal plane distance between the substrate and UME) and then moved laterally (Figure 2b) until it is centered right atop the particle of interest (in the center of the optical field of view, Figure 2c). Noteworthy, when the UME is centered atop the particle, the UME acting as a mirror reveals

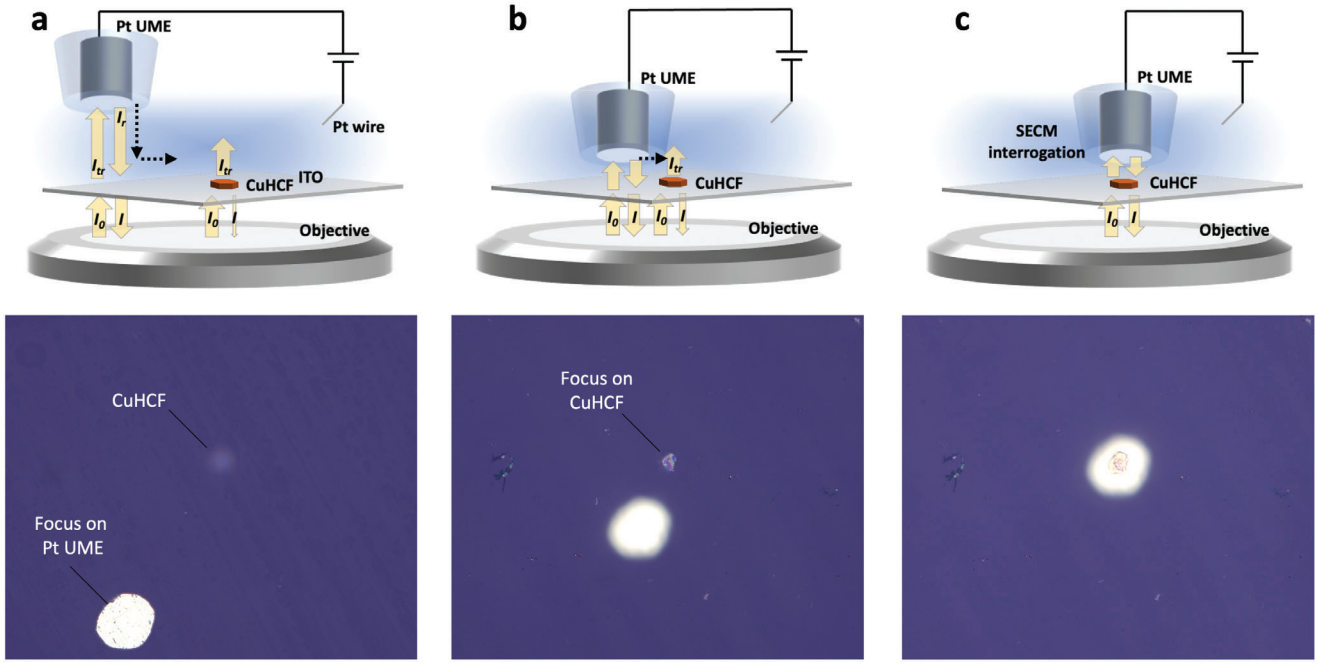

Figure 2. Schematic of the strategy employed to target and measure by optical microscopy-SECM the charge storage dynamics at a single solid booster CuHCF particle during redox exchange with a redox mediator. The sequence a–c) explains the protocol used for positioning the SECM Pt UME at a controlled height above a targeted CuHCF particle, with corresponding in situ full-field optical microscopy raw color images (175 × 150 μm^2); The optical microscopy first targets a particle (position locked from automatic motor control of the microscope platform). a) With a low magnification objective, the Pt UME is detected and approached roughly to the support (≈50–100 μm) and near the field of view of the particle of interest. The approach of the UME is monitored until it is at ≈10 μm from the support; b) focus on the substrate and lateral approach of the UME until it is centered with the particle c) from which SECM interrogation is triggered (see Figure 1); comparing (b, c) shows the change from reflection mode imaging to absorption mode imaging of the particle. The yellow arrows show the light paths, I_0 is the incident light and I is the light collected by the objective and camera, I_{tr} corresponds to the light transmitted through the substrate, and I_r is the light reflected by the metallic part of the UME acting as a mirror. Dashed black arrows show the motion of the UME.

a colored image of the particle (Figure 2c and Figure 1b), while when the particle is not covered by the UME, the optical image reveals the particle from its reflection of the illuminating light beam (showing interference patterns as in Figure S3, Supporting Information). Figure 1b presents a raw color optical image obtained of a particle targeted by the SECM tip and ready for electrochemical interrogation, revealing a single orange CuHCF object at the center of a luminous disk corresponding to the Pt wire of the UME held directly above it.

2.1.2. Color Optical Absorbance Imaging by Mirrored Epi-Illumination Microscopy

The Pt UME in our setup also serves a dual role, not only for local electrochemical probing but also as an optical mirror. When illuminated through the microscope objective (epi-illumination), it reflects the light beam that passes through the CuHCF particle. This reflected light, after a second passage through the particle (as illustrated in Figures 1a and 2) is directed back towards the objective and then to the color camera. In this configuration, made possible by the mirror-UME, we can probe the light transmitted through the particle, and consequently its absorbance. This technique is reminiscent of the trans-illumination configuration used to investigate electrochromic NPs, including PB nanocrystals.[21,38–42]

According to the schematic light paths presented in Figures 1a and 2, we can then evaluate from optical movies of the particle, here at a framerate of 20 frame per second (fps), the absorbance of light at any given time, $A(t)$, by a region of interest (ROI) within the imaged particle by comparing the intensity of light received in the presence ($I(t)$) and absence ($I_0(t)$) of the particle, using:

$$A(t) = \log\left(\frac{I_0(t)}{I(t)}\right) \quad (1)$$

Similar to macroscale spectroelectrochemical [23] or single-NP optical imaging studies,[36,38–43] this optical configuration allows us to investigate quantitatively and *operando* (electrochromic) redox transformations at individual CuHCF microparticles.

According to the Beer–Lambert law (details in Section S3, Supporting Information), the absorbance, A, provides a measurement of the quantity of absorbing material in both its oxidized and reduced forms.[56] Consequently, it offers insight into the local 2D state-of-charge of the particle, integrated over its entire thickness. It is worth noting that the same formalism applies to the absorbance variations of the solution layer separating the UME and the ITO surface. However, the low concentration of TEMPTMA (5 mM) compared to that of active centers in CuHCF

(≈6.45 M, see details below) renders the contribution of the solution to the measured absorbance variations negligible in this context.

With the aid of a color camera, which decomposes the image into three color channels (red, green, and blue, respectively denoted *r*, *g* and *b*, following the method outlined in, Section S4 (Supporting Information), we can then spectroscopically image the particle's absorbance and, consequently, its state of charge within each spectral range.

It is worth noting that due to matching refractive indices between the particle and the transparent ITO substrate, particles are much less visible in reflection mode, as observed in the image of the particle without the mirror-UME (Figure 2b; Figure S3, Section S3, Supporting Information). This reduced visibility makes reflection-based imaging much less sensitive, unlike what was previously proposed for probing Li-ion insertion in primary microparticles.[33,34,37] This is actually advantageous as by replacing the color camera with a fibered UV–vis spectrometer, we can capture the UV–vis absorbance spectrum of the entire individual CuHCF particle across the entire field of view. Figure 1c displays such spectrum from a single microparticle in its pristine state (≈60% reduced), featuring an extinction peak in the green at ≈565 nm, consistent with literature data.[57] The spectrum of the same particle in its oxidized state (see Figure S4, Section S3, Supporting Information) enables the evaluation of the spectroscopic absorbance variation (ΔA) during the particle's oxidation, as shown in Figure 1c. This plot is overlaid with the spectral ranges probed by the different color channels of the camera, revealing that the particle and its transformation are imaged more sensitively within the green channel (A_g).

2.1.3. SECM Probing of the Conversion of CuHCF Particles

In order to investigate the conversion of CuHCF particles in an SB-FB-like environment, we employ the Pt UME to initiate the redox conversion of an individual secondary particle, as illustrated in Figure 1a. At the start of the experiment, both the pristine CuHCF and TEMPTMA are in their reduced states, denoted $CuHCF^{(II)}$ and R, respectively. The amount of TEMPTMA is in excess compared to CuHCF, so it might reduce all the particles to their reduced state, the reduction should then not be controlled by the charge transfer kinetics. The Pt UME is then biased to a potential higher than $E^{\circ}_{TEMPTMA}$ (+0.91 V vs SHE), leading to the oxidation of TEMPTMA at the UME into species denoted O^+. The O^+ species formed at the tip subsequently diffuse into the electrolyte, eventually reaching the CuHCF particle (as well as the substrate). This leads to the oxidation of the $CuHCF^{(II)}$ component of the particle, converting it into $CuHCF^{(III)}$ while simultaneously regenerating R at the interface between the particle and the redox electrolyte. This oxidation process is accompanied by the deintercalation of K^+ ions from tetrahedral sites of the CuHCF structure, releasing them into the electrolyte. This oxidation process of the CuHCF particle corresponds to the forward step of Equation (2), or equivalently the charge of the CuHCF:

$$K_2Cu_3\left[Fe^{II}(CN)_6\right]_2 + 2O^+ \rightleftharpoons Cu_3\left[Fe^{III}(CN)_6\right]_2 + 2\theta + 2R + 2K^+ \quad (2)$$

where θ denotes the vacant K^+ sites within CuHCF.

To investigate this conversion process, cyclic voltammetry experiments are first conducted by sweeping the UME potential (E) from 0 to 1.2 V versus Pt. The evolution of absorbance, A_g, recorded in the green channel (integrated over a ROI within the particle as described in the methods section and Figure S5, Section S4.1, Supporting Information) as a function of UME potential is presented in Figure 1d (lower panel; corresponding evolutions in the blue and red channels are available in Figure S5, Supporting Information). The sigmoidal shape of the $A_g - E$ curve (also called absorptiogramm) closely mirrors the tip current variation, i_{tip}, along the sigmoidal voltammogram, recorded at the Pt UME tip during the oxidation of R (see upper panel of Figure 1d). This alignment confirms that the conversion of the particle occurs simultaneously with the formation of the oxidized form of the redox mediator (O^+). Moreover, this conversion process is also completed within the timescale of the cyclic voltammetry experiment, when R is totally converted (plateau current) at the UME. On the backward scan of the cyclic voltammetry, the O^+ species electrogenerated at the UME is converted back to R. Owing to the match between the E^0 of the TEMPTMA and CuHCF components, the presence of R in the vicinity of the particle yields the backward conversion of the particle (reduction or equivalently discharge of the particle). The reversibility of the particle's conversion is evident in the reverse scans of both curves, demonstrating that it is both rapid and reversible, primarily driven by the conversion of the redox electrolyte, O^+/R, at the UME.

2.2. Oxidation/reduction Dynamics at the Single-Microparticle Level

2.2.1. Electrochemical Titration via SECM

Given the different characteristic lengths and timescales involved in the oxidation/reduction of microparticles, we opt to investigate the dynamics of these processes through chronoamperometric experiments. These experiments involve monitoring the transient behavior of the tip current, i_{tip}, and the particle's absorbance, A_g, while maintaining a constant potential at the Pt UME. As depicted in the upper panel of **Figure 3a**, the particle is first oxidized for 100 s and subsequently reduced for another 100 s.

During the particle's oxidation, the Pt UME potential is held at E = 1.1 V (corresponding to the cyclic voltammetry plateau current, see Figure 1d), maintaining a steady delivery of O^+ under solution mass transfer control. In the subsequent reduction, the electrode potential is reverted to 0 V, restoring the particle's initial (most reduced) state of charge. Simultaneously, we record both the transient UME current and optical images of the individual particle. The corresponding sequence of optical images, taken at 20 fps, is provided as Movie S1 (Supporting Information) or, background subtracted for better visualization of the particle absorbance variation in Movie S2 (Supporting Information). Noteworthy, the electrochemical current at the UME provides information about the overall conversion of the particle because the size of the UME is larger than the particle. Electrochemical imaging of the local conversion of the particle would require a much smaller size UME than the particle. Due to the thickness of 3 to 4 µm of the particle, such an SECM interrogation at the nanoscale would be difficult to interpret quantitatively because

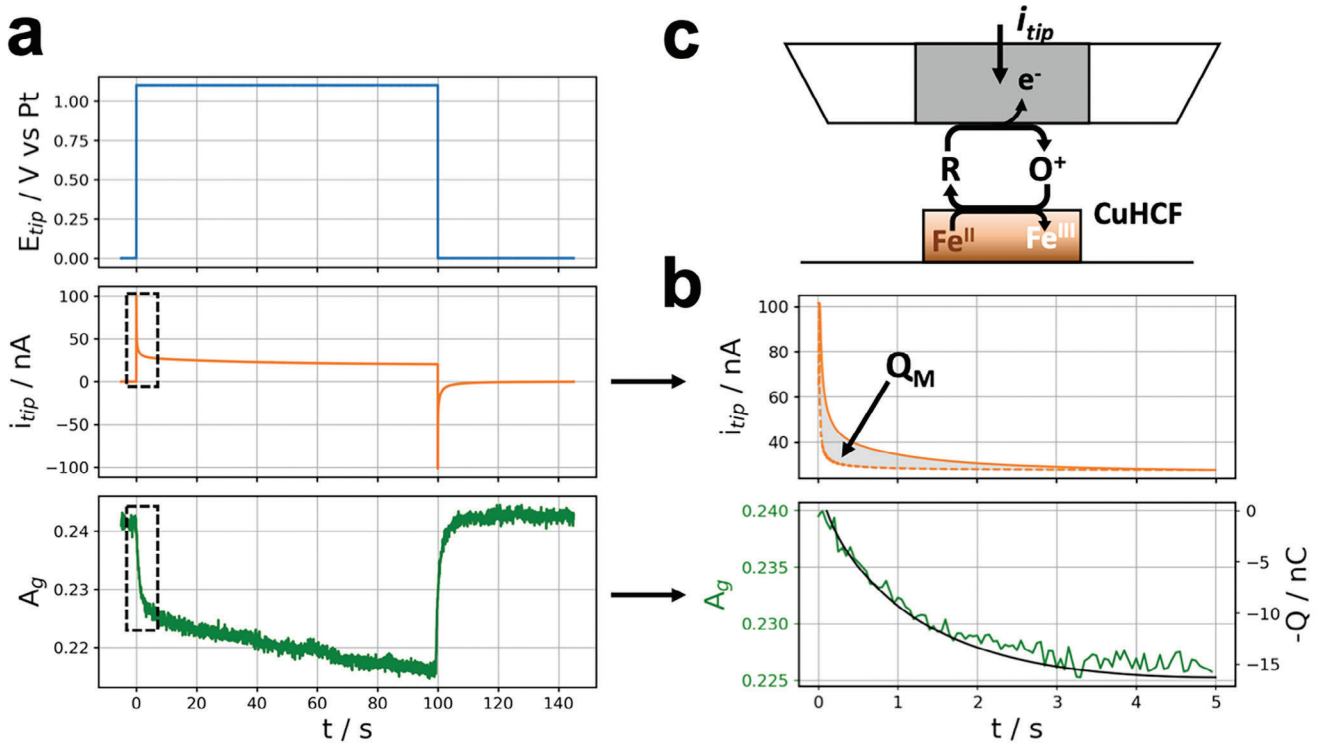

Figure 3. Analysis of single secondary CuHCF microparticle oxidation and reduction via SECM and optical microscopy. a) Upper panel: UME polarization procedure; middle panel: experimental current recorded at the UME, i_{tip}, in a solution containing 5 mM TEMPTMA (R) + 1 M KNO_3, enabling, in b) by comparison of i_{tip} in the absence (dashed line) and presence (solid line) of the particle, an estimation of the total exchanged electrochemical charge, Q_M; lower panel: global variation of the particle's absorbance probed from the optical images (green channel from Movie S1 (Supporting Information); see also background subtracted Movie S2, Supporting Information) as in Figure 1d, compared in (b) with the instantaneous electrochemical charge, Q, represented by the black line. c) Scheme showing the charge exchanged with the particle (during oxidation) associated with R regeneration revealed by the UME current response, i_{tip}. Inset: zoomed regions analyzed in (b).

it would hardly allow the entire thickness of the particle to be probed. Here, we further take advantage of the use of a 25 µm large UME, relative to the particle, to electrochemically interrogate the entire particle, while the local conversion is monitored through optical images. These images enable us to evaluate both the global absorbance of the particle and its local absorbance (at the individual pixel level) using Equation 1. In this section, we compare the global optical response with the UME's current response in **Figure 4**, providing insight into the particle's overall (average) conversion dynamics in relation to its electrochemical response. Next, this comparison will serve as a basis for later analyzing the local optical response in terms of local state-of-charge, as discussed in Section 2.3, which also yields sub-particle (submicrometer) spatial resolution images of the oxidation/reduction dynamics.

Chronoamperometric experiments were conducted in both 1 and 0.01 M KNO_3, as presented in Figure 3 and Figure S6 (Supporting Information) (Section S4, Supporting Information), respectively. Figure 3a illustrates the potential program applied to the UME tip (upper panel) along with the recorded current, i_{tip} (middle panel), and the averaged optical response (lower panel) captured in the green channel over a 2.75 × 2.75 µm² ROI of the CuHCF particle.

In Figure 3b, the recorded tip current (solid orange line) is compared to the background tip current (dashed orange line), extrapolated from measurement performed in a particle-free region of the ITO substrate (procedure detailed in Section S4.2, Supporting Information). In the absence of particles, the background tip current decays rapidly towards a quasi-steady-state value. However, over the particle, the current exhibits an additional transient at short times, within the first 2 s of the experiment. This transient is characteristic of the regeneration of R by the CuHCF particle, as indicated by Equation (2) and schematized in Figure 3c.

The influence of electrolyte K^+ concentration is evident in the oxidation behavior of a different particle in 0.01 M KNO_3 (see Figure S6, Supporting Information). With reduced K^+ concentration, the oxidation is even faster, generating a current transient for only ≈1 s under constant current before decaying to the background current. Lower K^+ concentration promotes faster K^+ outflow from the particle, while a constant current reduction indicates a limitation imposed by the transport of the redox mediator in solution. Additionally, due to the reduced K^+ concentration, the reduction reaction (K^+ insertion) is hindered and significantly slower than the oxidation.

These measurements are then used for quantitative assessment of the oxidation/reduction process, in line with the SI-SECM mode methodology.[24,25] We integrate the observed supplemental tip current over time (as indicated by the grayed region between both curves in Figure 3a) to determine the electrochemical charge, $Q(t)$, exchanged during the particle's

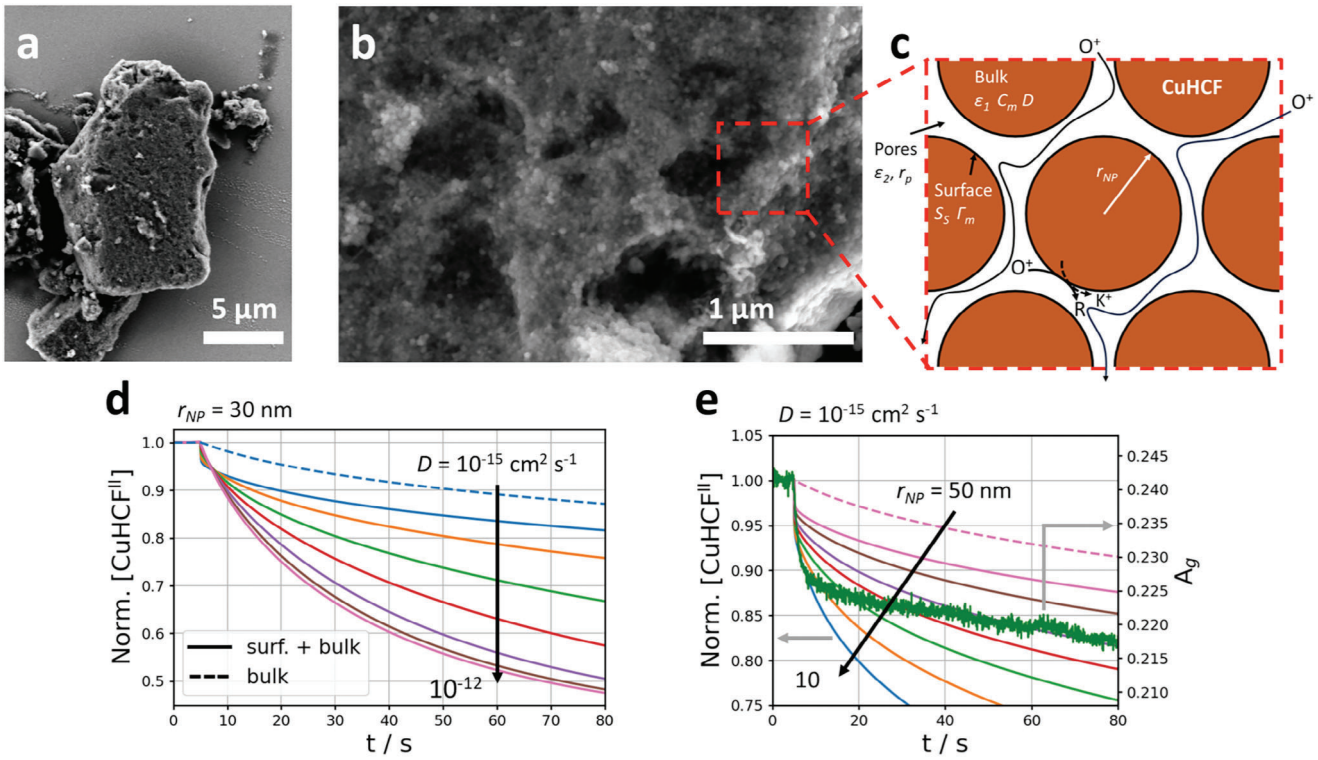

Figure 4. Experimental evidence accounting for the porous nature of the CuHCF microparticles a, b): SEM images showing the porous structure of the secondary particle formed from agglomerated primary particles (nanocrystals) as studied in Figures 1 and 2. c–e) Simulating SECM potentiostatic oxidation of secondary porous CuHCF microparticle (see Section S7, Supporting Information). c) Schematic description of the model accounting for reaction-transport of redox shuttle O^+ in a porous network: the microparticle is made of spherical nanocrystals (radius r_{NP}) in a cubic close-packed network separated by voids defining the porosity volume (with porous and solid volume fractions respectively ϵ_2 and $\epsilon_1 = 1 - \epsilon_2$ and apparent pore radius r_p). The nanocrystal's conversion (with bulk or surface concentration of electroactive material C_m or Γ_m) takes into account surface conversion and a diffusive conversion (shell-to-core) towards the core of the NPs. d) Example of COMSOL simulated microparticle-volume-averaged conversion for different K^+ solid-phase diffusion coefficients $D = 10^{-12}$, $3\ 10^{-13}$, 10^{-13}, $3\ 10^{-14}$, 10^{-14}, $3\ 10^{-15}$, and 10^{-15} $cm^2\ s^{-1}$ considering either the conversion of the surface+bulk of the nanocrystals (solid lines) or only the bulk conversion of the nanocrystals (dashed lines) for 30 nm radius nanocrystals; e) Example of microparticle-volume-averaged simulated conversion for packing of nanocrystals of different radii r_{NP} = 10, 15, 20, 25, 30, 40, and 50 nm (see also Section S7, Supporting Information) compared with the experimental absorbance variations (green curve, right axis) suggesting a reasonable agreement for $D = 10^{-15}$ $cm^2\ s^{-1}$ and $r_{NP} \approx 30$ nm, in agreement with the STEM image in Figure S2-2, Section S2 (Supporting Information).

oxidation. A similar analysis can be done for the particle's reduction as demonstrated in Figures S7 and S8, Section S4 (Supporting Information). Over the initial $t < 5$ s of the particle's oxidation process (or $t < 15$ s for reduction), we find that the electrochemical charge, $Q(t)$, plotted against time, t, can be described by an exponential function:

$$Q\ (t) = Q_M\ \left(1 - \exp\left(-k_{app}t\right)\right) \quad (3)$$

This expression allows us to derive two crucial parameters: Q_M, which represents the total electrochemical charge exchanged during the SECM interrogation and k_{app}, which represents the characteristic conversion rate.

From the curves presented in Figure 3b, we determine that $Q_{M,ox} = 18\ nC$. Interestingly, a greater electrochemical charge of $|Q_{M,red}| = 27\ nC$ is obtained during the reduction process. As will be discussed later on, our optical absorbance monitoring, presented in the lower panel of Figure 3a, reveals the reversibility of the particle's conversion throughout the entire oxidation/reduction cycle. The discrepancy in Q_M values suggest that both processes follow distinct dynamics. Notably, the particle's oxidation unfolds across two different timescales. After an initial rapid oxidation (t < 5s), it undergoes a deeper oxidation over a more extended duration. It is worth noting that this latter trend, clearly visible in the transient absorbance variation (lower panel of Figure 3a), is not entirely captured in the electrochemical charge transient due to its dependence on curve subtraction methods (further details in Section S4 and Figures S7 and S8, Supporting Information).

To understand the depth of conversion, we refer to the largest measured electrochemical charge of 27 nC, which corresponds to the conversion of an equivalent of 0.14 pmol of $K_2Cu_3[Fe^{II}(CN)_6]_2$ sites, or equivalently 0.28 pmol of $[Fe^{II}(CN)_6]$ sites, according to Reaction 2. Given the structural analogy of CuHCF with PB, we can ascertain that the cubic face centered unit cell of 10.1 Å contains two $K_2Cu_3[Fe^{II}(CN)_6]_2$ unit. Consequently, the maximum concentration of $[Fe^{II}(CN)_6]$ sites (twice more than $K_2Cu_3[Fe^{II}(CN)_6]_2$ units) within a fully reduced particle is C_m = 6.45 m.[13] We can then estimate the initial quantity of $[Fe^{II}(CN)_6]$ sites within the particle using the particle's geometrical

volume, which we approximate as $V \approx 260\ \mu m^3$. This volume is determined based on the average particle height, 3 μm, obtained from the 3D reconstruction of SEM images (see Figure S2, Section S2, Supporting Information) and the particle's projected surface area. Neglecting first the porosity of the analyzed particle, considering it as a single solid phase microparticle, it would comprise in its fully reduced state $n^0_{Red} = C_m\ V\ =\ 1.6$ pmol of $[Fe^{II}(CN)_6]$ sites. The pristine analyzed particle, based on a 61% reduced state, then contains $n^0_p = 0.61 C_m\ V\ =\ 0.98$ pmol of $[Fe^{II}(CN)_6]$ sites, from which we deduce that only a small fraction (29%) of these sites undergo conversion during the SECM experiment.

2.2.2. Spectroscopic Titration Using Optical Microscopy

The absorbance variations, A_g, recorded in the green channel (other channels displayed in Figure S6, Supporting Information) and averaged over a 2.75 × 2.75 μm² ROI within the particle during oxidation and reduction, are presented in the lower panel of Figure 3a. The oxidation exhibits a distinct pattern, with a rapid initial conversion at short times followed by a slower decay of the absorbance at longer times ($t > 10\ s$). The rapid initial oxidation, highlighted in the lower panel of Figure 3b, closely mirrors the dynamics of the electrochemical charge, Q. This observation suggests a linear relationship between Q and A_g which will later facilitate the conversion of optical images into local state-of-charge images. As for Q, the dynamics of A_g in the $t\ <\ 5\ s$ range can then also be described by an exponential variation (Equation 4). This exponential variation of the particle's absorbance further supports the trends observed during the conversion of single PB NPs.[39]

$$A_g\ (t) = A_{g,bg}\ + \Delta A_g \exp\left(-k_{app} t\right) \tag{4}$$

where $A_{g,bg}$ is the background absorbance before the oxidation potential pulse and ΔA_g is the total absorbance variation compared to $A_{g,bg}$, here all considered in the green channel of the camera.

It is noteworthy that this equation enables the quantification of the initial fast oxidation and reduction rates which are rather similar ($k_{app} =\ 1.1\ s^{-1}$). A slower conversion of the particle is also noticeable at a longer time, both during oxidation and reduction. Empirically, this slower conversion can be fitted by incorporating a second exponential function into Equation 4, with rates of ≈0.02 and 0.25 s^{-1} for oxidation and reduction, respectively.

2.2.3. Modeling the Conversion of Single CuHCF Particles—Role of Particle Porosity

We then conducted finite element simulations, using COMSOL, to simulate the potentiostatic oxidation/reduction experiment in the SECM configuration, focusing first on a model monocrystalline micrometric cylindrical particle. Additional details about the simulations and their discussion are available in Sections S5.1 and S5.2 (including Figures S9–S13) Supporting Information). In summary, these simulations indicate that both the tip current transient and the average particle conversion follow an exponential variation with time, as observed experimentally through Equations 3 and 4. However, even when employing the highest reported solid-state ion diffusion coefficient value ($D\ =\ 1.5\ 10^{-9}\ cm^2 s^{-1}$),[12] the simulated transients remain approximately eight times slower than the experimental ones. Interestingly, increasing D values did not significantly accelerate the conversion dynamics. Higher D values would only shift the conversion regime from a solid-state diffusion control to control by the mass transport of R/O^+ in solution, considering the low concentration of the redox mediator in solution compared to that of CuHCF species in the solid phase. Furthermore, the simulation predicts a particle conversion of over 60%, significantly higher than the experimental value of 29%.

The incomplete and relatively rapid conversion of the particle can be attributed to the porous nature of the CuHCF particle. These materials are usually not solid microcrystals but rather assemblies of primary nanocrystals (in the 20–50 nm range),[13] as confirmed here by high-magnification SEM images in **Figures** 4a,b (see additional images in Section S2, Supporting Information). These images reveal irregularities and grains within the particle, conferring it a porous structure. This porosity should favor the surface-confined conversion of the primary nanocrystal rather than their volume conversion, which is the reason why porous PBAs are also used in supercapacitor applications.[58]

Recent studies have demonstrated the surface-confined transformation of PBAs through single-nanocrystal optical analysis.[40] Inspecting the conversion mechanism at the individual building block level (single primary nanocrystal) allows for the removal of the effect of porosity and hence to investigate only ion diffusion within the crystalline structure. These studies have suggested at least three orders of magnitude smaller K^+ diffusion within PB nanocrystals, which is more consistent with the 10^{-12}–10^{-15} $cm^2\ s^{-1}$ values reported.[39,40,59] Within the first t_i = 5 s of our experiment, such slow K^+ diffusion would result in a capacitive-like electrochemical conversion involving only a thin shell (about $\sqrt{Dt_i}$ in the 0.7–20 nm range) of the nanocrystals. This surface process likely plays a significant role in the conversion of porous secondary particles formed from agglomerated primary particles.

Additionally, we confirmed the porosity of the CuHCF microparticles by measuring N_2 adsorption/desorption isotherms analyzed within Brunauer Emmet and Teller (BET) framework. This analysis (detailed in Section S6, Figures S14 and S15, Supporting Information) suggests the presence of micro- and mesoporosity with an average pore diameter of ≈9 nm and a specific mesoporous surface area, $S_{SA} \approx 10^2\ m^2\ g^{-1}$. Using the specific surface area, we can estimate (details in Section S6, Supporting Information) that the 260 μm³ CuHCF particle, consists of ≈13% of $[Fe^{II}(CN)_6]$ surface sites. This value twice smaller than the conversion measured by electrochemistry (see above), implies that the observed electrochemical conversion would mostly consist of the conversion of a thin shell (2 cell-units) or surface sites of the porous network, which is consistent with single PB nanocrystals conversion studies.[40]

To further investigate the role of porosity, we incorporated it into our simulations (see Figures 4c–e and simulation details in Section S7, Figures S16 and S17, Supporting Information). These simulations modeled the microparticle as a porous assembly of nanosized primary particles (nanocrystals), as proposed for modeling ion insertion in porous battery electrodes,[60] considering their surface and bulk conversion. Figure 4d demonstrates the impact of the K^+ diffusion coefficient inside the CuHCF

crystal (D) on the particle's average conversion dynamics. Higher D values make surface conversion negligible (compare solid and dashed lines for $D = 10^{-12}$ cm^2 s^{-1}), while lower D values make surface conversion predominant (compare solid and dashed lines for $D = 10^{-15}$ cm^2 s^{-1}). Figure 4e and Figure S17 (Supporting Information) explores the influence of the nanocrystals' size on the conversion dynamics, showing additionally that larger nanocrystals produce a faster initial surface conversion, followed, at longer times, by a slower bulk-like conversion.

In summary, the simulations presented in Figure 4 effectively replicate the experimental observations, meaning both the incomplete conversion of the particle and the initial rapid conversion followed by a slower one at longer times. The initial rapid conversion ($t < 5$ s) is attributed to the surface conversion of the nanosized primary particles, while the slower, deeper conversion at longer times corresponds to the bulk conversion of primary particles. This behavior is closely linked to the transport of the redox electrolyte in the porous secondary particle formed from the assembly of nanosized primary particles. While the model simplifies certain aspects, such as the distribution of primary particle sizes which is considered perfectly monodisperse, and the porosity which is considered perfectly uniform over the particle, it aligns well with our experimental observations. In Figure 4e, the experimental conversion dynamics in terms of absorption are also displayed along the simulated curves. It matches at short and longer times with the simulation considering an assembly of 30 nm-radii nanocrystals with interparticle porosity and a solid-state ion diffusion coefficient, D, of the order of 10^{-15} cm^2 s^{-1}, within the range of some reported values for PBA nanocrystals.[59] The simulations indicate that mass transfer within the solid is the limiting factor in the current experimental configuration, with the redox exchange charge transfer rate coefficient higher than 0.1 cm s^{-1}. As the model is able to reproduce the experimental results, this gives us a design tool to predict the effect of various parameters such as primary particle size, porosity, electrolyte convection, etc., but also to discuss kinetic limitation by the charge transfer rate, on the system performance in the scale of realistic system where particles are deposited in the tank of a flow battery.

2.3. Sub-Particle Imaging of the Oxidation/Reduction Dynamics

We can now leverage the proportionality between Q_M and ΔA_g discussed at the global/particle scale to scrutinize local phenomena occurring within the particle. By transforming the local absorbance data, a_g, captured by optical microscopy into local electrochemical charge density, q, we gain additional mechanistic insights into the microparticle's conversion with sub-particle (sub-micrometer) imaging resolution. This local analysis is presented as a series of spatial maps presented in Section S8 (Figures S18-1–S18-6) Supporting Information for the different experimental configurations explored. Regarding the chronoamperometric experiment discussed in Figure 3, spatial maps of the oxidation and reduction of the entire particle are provided in Figure S18-1 (Supporting Information). For a more precise picture, we provide a zoomed-in view (5×7.5 µm^2, ≈1/3 of the particle) of the upper-right part of the particle during the oxidation process in **Figure 5**.

2.3.1. From Local Loading to Local Charge Density

Figure 5a presents a map of the optical contrast, in the green channel, of the particle. This descriptor, represented by $a_{g,bg}$ in Equation 4, is actually reminiscent of the pristine particle and reflects the local loading of the particle with absorbing materials: regions with higher $a_{g,bg}$, i.e., which absorb more, and contain greater amounts of CuHCF. This can mean that either the particle is thicker in this region or that primary particles are more densely packed. In this framework, the red contours in Figure 5a highlight regions of high material loading ($a_{g,bg}$), while the white contours highlight selected regions of low material loading.

Then, the local dynamics of the particle's conversion are revealed in Figures 55b-d. To create these maps, we fitted the time profiles of each pixel obtained from the absorbance movies with an exponential function according to Equation 4 (see Section S4.4, Supporting Information). This fitting procedure reveals the spatial distribution of both the local conversion rates (k_{app}) and the local electrochemical charge stored in the particle (q_M expressed in mC cm^{-2} as opposed to Q_M which is expressed in nC).

Figure 5b depicts the maximum local electrochemical charge, q_M, stored in the particle and evacuated during the oxidation step (evaluated from the fitting parameter Δa_g).

If material loading is heterogeneously distributed in Figure 5a, it is expected that the map of local electrochemical charge, q_M, is also heterogeneous. Indeed, the higher the loading, the higher the amount of electrochemical charge that can be stored. This correlation is generally observed across the entire particle as shown in the scatter plot presented in Figure S19a (Section S9) Supporting Information, where q_M versus $a_{g,bg}$ is explored over all pixels of the imaged microparticle.

However, despite this general trend, Figure 5a,b reveals that this correlation does not hold uniformly in all regions of the microparticle. For instance, region #2 marked by a white contour on the left edge of Figure 5a exhibits relatively low loading but stores as much electrochemical charge as the surrounding matrix. Similarly the low loading region #1 near the upper edge of the particle shows (yellow) regions with up to twice the higher charge storage capacity. These local behaviors suggest the presence of regions with higher porosity or smaller nanocrystals, enabling deeper bulk conversion.

2.3.2. Differentiating Local Surface Versus Bulk Conversion

Next, the conversion rate maps revealed in Figures 5c,d are used to discuss the local oxidation rate of the particle. To differentiate surface and bulk primary particle conversion dynamics, instead of using two exponential functions which would complicate the fitting procedure, we evaluated the conversion rates using either the first 5 s (k_{app}^{5s}) or the first 15 s (k_{app}^{15s}) of the absorbance variations after the potential pulse. As established earlier and supported by the simulations, the 5 s-fit captures the rapid initial surface conversion of the nanocrystals, while the 15 s-fit describes the deeper and slower bulk conversion. The k_{app}^{5s} values would then be more likely to reveal capacitive-like behavior, while battery-like behavior would be more prominent in the k_{app}^{15s} values.

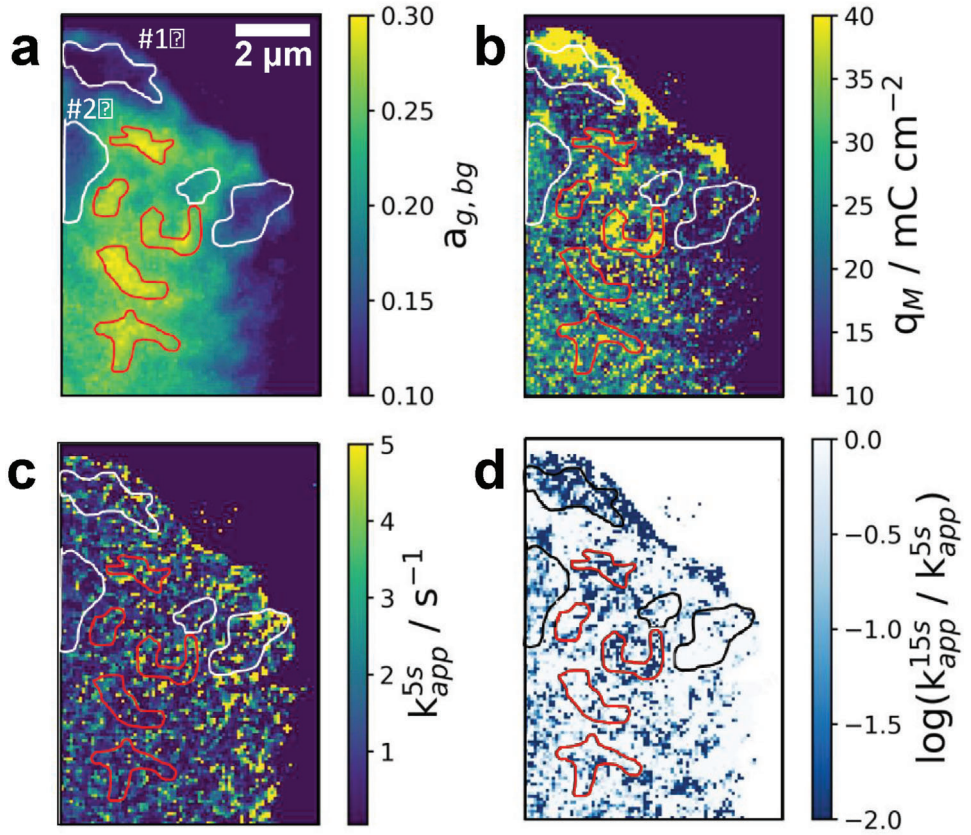

Figure 5. Imaging the local oxidation within a single secondary CuHCF particle. From the raw optical images of the particle in its pristine state, in a) the local absorbance variations (local loading) are converted into b) local electrochemically stored charge and c, d) local oxidation rates. The conversion rates in (c) and (d) are evaluated by fitting the absorbance variations according to Equation 4 either using the first 5 s (fast oxidation analyzed) or 15 s (slow oxidation analyzed) after the potential pulse. In d), the ratio of the apparent oxidation rates $k^{15s}_{app}/k^{5s}_{app}$, slow versus fast oxidation rate (bulk vs surface), is mapped (original k^{15s}_{app} map can be found in Section S8, Figure S18-1, Supporting Information).

Figure 5c highlights the map of the initial rapid surface conversion. While Figure 5a reveals regions of contrasting loadings, the short-time conversion rate maps (5 s images in Figure 5c, or equivalently for the reduction in Figure S18-1d, Supporting Information) appear relatively uniform across the particle, with an average oxidation rate of ≈2 s^{-1}. From Figure S18-1d (Supporting Information), the short-time reduction is also homogeneous with a slightly faster average reduction rate of ≈4 s^{-1}. During these initial moments, the conversion primarily occurs on the surface of the porous network, thus indicating a homogeneous local capacitive-like conversion with a homogeneous specific surface area across the particle.

Conversely, the long-term conversion maps (15 s images in Figure S18-1, Supporting Information) unveil regions of more contrasted kinetics. This is captured from Figure 5d through a comparison of the rate of oxidation evaluated at 15 s versus that evaluated at 5 s. This image thus conveys the extent of local bulk versus surface (battery vs capacitive) conversion across the particle, with darker regions revealing regions experiencing deeper and slower bulk oxidation (battery-like behavior).

With k^{15s}_{app} values up to 100 times slower than the surface conversion rates, k^{5s}_{app}, Figure 5d suggests heterogeneity in access to bulk CuHCF. This observation aligns with the heterogenous maps of material loading or electrochemical charge ($a_{g,bg}$ or q_M) presented in Figure 5a,b.

The global analysis and simulations from the previous sections indicated that the deeper conversion of CuHCF involved slower conversion rates (more visible during the oxidation process because of the high electrolyte K^+ concentration). This trend is then expected to be revealed on the maps as well: regions that store higher amounts of electrochemical charge q_M should also exhibit slower conversion rates. A correlation, pixel-by-pixel, between local q_M and local oxidation rate, k^{15s}_{app}, can indeed be observed when considering the long-time conversion rates. The corresponding scatter plot is shown in Figure S19b (Section S9) Supporting Information.

However, it is worth noting that this correlation again does not hold uniformly across all regions of the microparticle. Some exceptions arise as seen in Figure 5d within regions of low material loading (as discussed earlier) such as regions #1 and #2. In these regions, the local electrochemical charge (q_M) appears to influence the conversion rates more strongly than material loading ($a_{g,bg}$). Interestingly, within these specific regions, areas characterized by a higher electrochemical charge exhibit slower and

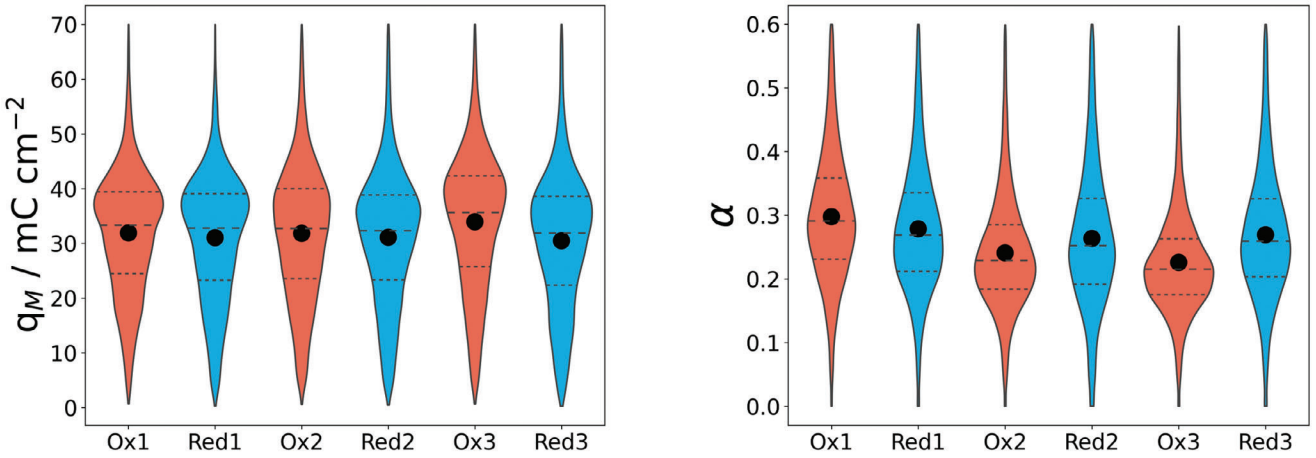

Figure 6. Violin plots showing the evolution of the distribution of the local charge transferred and α, the dimensionless local conversion rate, over the whole particle along three oxidation/reduction cycles during CV. The violin for oxidation (red) or reduction (blue) is provided with their interquartile values, Q1, Q2 (median), and Q3, as dashed horizontal lines and the mean values as disk symbols.

deeper oxidation. These optical maps thus unveil mechanistically relevant behaviors, potentially linked to the local nanostructure or porosity of the particle. For instance, regions with lower loadings but high electrochemical charge such as regions #1 and #2 may reveal regions with higher porosity or smaller nanocrystals, which promote deeper bulk conversion.

2.3.3. Local Behavior Upon Successive Oxidation/Reduction Cycles

Successive oxidation/reduction cycles can then be analyzed through this imaging strategy. By cyclic voltammetry (CV) experiments conducted in 1 M KNO_3, three subsequent oxidation/reduction cycles of TEMPTMA at the Pt UME were performed above the same particle. Similar to Figures 3 and 5, the electrochemical responses are given in Figure S18-2 (Supporting Information), while the optical images (Figure S18-4, Supporting Information) were analyzed globally for changes in particle absorbance and locally via pixel-by-pixel optical analysis. The local and global analysis is provided in Section S8 (Supporting Information). It confirms the trends observed during the CA experiments and discussed in Section 2.3.2., namely there is a general tendency to suggest that the greater the charge injected in or removed from the particle, the slower the process (the more it will reach the bulk of individual nanocrystals within the particle). This is illustrated in the maps of Figure S18-4 (Supporting Information), analogous to those of Figure 5, showing that regions where a higher amount of charge, q_M, is stored or removed during oxidation or reduction are also regions where the charge is stored or removed for a longer period of time.

Figure 6 presents a statistical analysis of the distribution of the exchanged charge q_M and of the descriptor of the particle conversion rate, denoted α (see Equation S-4 in Section S4.4, Supporting Information, the higher α, the faster the conversion), based on the set of pixels of the particle and along the successive oxidation/reduction cycles in the form of violin plots. The figure also shows the evolution during these cycles of the interquartile (dashed horizontal lines) and mean values (symbols) of the distribution. Over the cycles, the evolution of the charge distribution suggests a certain loss of reversibility. This is because the particle seems to be more oxidized over the cycles while the reduction becomes less effective. Again, the opposite trend is observed for the conversion rate of the process, and the dynamics of the oxidation process also becomes slower, because α decreases over the oxidation cycles, while it is almost unchanged over successive reduction steps. This suggests a deeper conversion of the bulk of the nanocrystals during oxidation (tending towards a battery-like behavior) while the reduction appears more constrained at the surface of the nanocrystals (capacitive-like behavior). A consequence of such loss of reversibility on cycles is also detected in local image analysis from the maps provided in Figure S18-4a (Supporting Information). In particular, some regions can show a loss of activity during the second cycle compared to the first cycle, but interestingly this activity can be recovered during the next third cycle. This could be interpreted as the clogging/unclogging of the redox mediator and K^+ transport and of the beneficial effect of porous nanostructure for unclogging mass transfer.

3. Conclusion

In this study, we have investigated the intricate oxidation/reduction dynamics of secondary CuHCF microparticles composed of nanoscale primary particles proposed as solid boosters in next-generation flow batteries. Our approach combined SECM and high-spatial-resolution optical microscopy to shed light on the oxidation/reduction behavior of CuHCF particles both at the global and local scale.

On the one hand, SECM allowed to target individual particles and monitor their conversion at the global scale, providing a rationale for the conversion of the optical signal into a state-of-charge. On the other hand, optical microscopy allowed imaging (spectroscopically) the conversion at the sub-particle (sub-micrometer) level revealing heterogeneous regions within the particle that likely originate from a locally higher porosity or smaller nanocrystal size distribution. Absorbance measurements, which are key for the quantitative assessment of battery

materials,[23] are made possible in epi-illumination by the presence of the UME which acts as an optical mirror. Indeed, various battery electrode materials are electrochromic [36] or present color change upon charge storage (most metal oxides, sulfur, etc.), and the described strategy could be employed to decipher charge storage processes or loss of electrode capacity.

Absorption reactivity maps highlight the spatio-temporal dynamics of the electrochemical conversion of porous secondary particles formed from agglomerated primary particles. They clearly evidence a homogeneous surface conversion (capacitor-like behavior) of nanocrystallites a short time followed by their slower and more heterogeneous bulk conversion (battery-like behavior). The later heterogeneity was uniquely probed from the optical maps highlighting the critical role of the local porosity of the material, which is further confirmed by COMSOL simulations of the full experimental configuration.

High throughput operando imaging and quantifying the role of porosity on the electrochemical conversion of secondary particles offer significant potential to advance our understanding of energy storage mechanisms in nanostructured electrode materials. Exploiting further this screening methodology should provide a rationale for the design of new porous materials for energy storage devices. Moreover, predictive models taking into account the effects of porosity, etc. will allow engineering of the materials in device scale to enable for example high power or high energy applications.

Supporting Information

Supporting Information is available from the Wiley Online Library or from the author.

Acknowledgements

M.M. and L.G. contributed equally to this work. M.M. acknowledges TOP-Säätiö, the Finnish Cultural Foundation, the Finnish Academy of Science and Letters, and the French Institute in Finland for supporting this work through Varsinais-Suomi, Väisälä, and Maupertuis funds. This work was partially financially supported through the CNRS and Université Paris Cité. The authors acknowledge the ITODYS SEM facility, the Ile-de-France region, and IDEX for financial support of the AFM-Beam-Rex platform, and ENS Paris-Saclay for PhD scholarship. P.P. and J.J. acknowledge funding from the European Research Council through a Starting Grant (agreement no. 950038), and M.M. and P.P. acknowledge the Academy Research Fellow funding by the Research Council of Finland (Grants No. 343794 and 343791). This work was supported by the Materials Research Infrastructure (MARI) at the University of Turku.

Conflict of Interest

The authors declare no conflict of interest.

Data Availability Statement

The data that support the findings of this study are available from the corresponding author upon reasonable request.

Keywords

flow batteries, nanoelectrochemistry, operando imaging, optical microscopy, reaction transport in porous media

Received: October 23, 2023
Revised: April 8, 2024
Published online:

[1] T. Janoschka, N. Martin, M. D. Hager, U. S. Schubert, *Angew. Chem., Int. Ed.* **2016**, *55*, 14427.
[2] Z. Zhao, X. Liu, M. Zhang, L. Zhang, C. Zhang, X. Li, G. Yu, *Chem. Soc. Rev.* **2023**, *52*, 6031.
[3] Q. Huang, Q. Wang, *ChemPlusChem.* **2015**, *80*, 312.
[4] S. Gentil, D. Reynard, H. H. Girault, *Curr. Opin. Electrochem.* **2020**, *21*, 7.
[5] J. Ye, L. Xia, C. Wu, M. Ding, C. Jia, Q. Wang, *J. Phys. D. Appl. Phys.* **2019**, *52*, 443001.
[6] Y. Chen, M. Zhou, Y. Xia, X. Wang, Y. Liu, Y. Yao, H. Zhang, Y. Li, S. Lu, W. Qin, X. Wu, Q. Wang, *Joule.* **2019**, *3*, 2255.
[7] T. Páez, F. Zhang, M. Á. Muñoz, L. Lubian, S. Xi, R. Sanz, Q. Wang, J. Palma, E. Ventosa, *Adv. Energy Mater.* **2022**, *12*, 2102866.
[8] E. Zanzola, C. R. Dennison, A. Battistel, P. Peljo, H. Vrubel, V. Amstutz, H. H. Girault, *Electrochim. Acta.* **2017**, *235*, 664.
[9] M. Zhou, Y. Chen, Q. Zhang, S. Xi, J. Yu, Y. Du, Y.-S. Hu, Q. Wang, *Adv. Energy Mater.* **2019**, *9*, 1901188.
[10] Z. Qi, G. M. Koenig jr., *J. Vac. Sci. Technol. B.* **2017**, *35*, 40801.
[11] M. Z. Bazant, *Faraday Discuss.* **2023**, *246*, 60.
[12] H. Kahlert, U. Retter, H. Lohse, K. Siegler, F. Scholz, *J. Phys. Chem. B.* **1998**, *102*, 8757.
[13] C. D. Wessells, R. A. Huggins, Y. Cui, *Nat. Commun.* **2011**, *2*, 550.
[14] M. Moghaddam, S. Sepp, C. Wiberg, A. Bertei, A. Rucci, P. Peljo, *Molecules.* **2021**, *26*, 2111.
[15] J. F. Vivo-Vilches, A. Nadeina, N. Rahbani, V. Seznec, D. Larcher, E. Baudrin, *J. Power Sources.* **2021**, *488*, 229387.
[16] R. Yan, J. Ghilane, K. C. Phuah, T. N. Pham Truong, S. Adams, H. Randriamahazaka, Q. Wang, *J. Phys. Chem. Lett.* **2018**, *9*, 491.
[17] Z. T. Gossage, N. B. Schorr, K. Hernández-Burgos, J. Hui, B. H. Simpson, E. C. Montoto, J. Rodríguez-López, *Langmuir.* **2017**, *33*, 9455.
[18] T. S. Watkins, D. Sarbapalli, M. J. Counihan, A. S. Danis, J. Zhang, L. Zhang, K. R. Zavadil, J. Rodríguez-López, *J. Mater. Chem. A.* **2020**, *8*, 15734.
[19] M. Burgess, K. Hernández-Burgos, K. J. Cheng, J. S. Moore, J. Rodríguez-López, *Analyst.* **2016**, *141*, 3842.
[20] P. Marzak, P. Moser, S. Schreier, D. Scieszka, J. Yun, O. Schneider, A. S. Bandarenka, *Small Methods.* **2019**, *3*, 1900445.
[21] R. C. Evans, Z. Nilsson, B. Balch, L. Wang, J. R. Neilson, C. R. Weinberger, J. B. Sambur, *ChemElectroChem.* **2020**, *7*, 753.
[22] N. Yang, S. Yu, W. Zhang, H.-M. Cheng, P. Simon, X. Jiang, *Adv. Mater.* **2022**, *34*, 2202380.
[23] D. Zhang, R. Wang, X. Wang, Y. Gogotsi, *Nat. Energy.* **2023**, *8*, 567.
[24] J. Rodríguez-López, A. J. Bard, *J. Am. Chem. Soc.* **2010**, *132*, 5121.
[25] N. B. Schorr, Z. T. Gossage, J. Rodríguez-López, *Curr. Opin. Electrochem.* **2018**, *8*, 89.
[26] B. Tao, E. Daviddi, L. Yule, C. L. Bentley, P. Unwin, *Angew. Chem., Int. Ed.* **2019**, *26*, 4654.
[27] B. Tao, I. J. McPherson, E. Daviddi, C. L. Bentley, P. R. Unwin, *ACS Sustain. Chem. Eng.* **2023**, *11*, 1459.
[28] G. Zampardi, C. Batchelor-McAuley, E. Kätelhön, R. G. Compton, *Angew. Chem., Int. Ed.* **2017**, *56*, 641.
[29] S. Goines, J. E. Dick, *J. Electrochem. Soc.* **2020**, *167*, 037505.
[30] E. B. Tetteh, D. Valavanis, E. Daviddi, X. Xu, C. S. Santos, E. Ventosa, D. Martín-Yerga, W. Schuhmann, P. R. Unwin, *Angew. Chem., Int. Ed.* **2023**, *62*, e202214493.
[31] X. Xu, D. Valavanis, P. Ciocci, S. Confederat, F. Marcuccio, J.-F. Lemineur, P. Actis, F. Kanoufi, P. R. Unwin, *Anal. Chem.* **2023**, *95*, 319.

[32] N. A. Gvozdik, A. A. Kurbatova, N. A. Ovsyannikov, M. A. Pogosova, K. J. Stevenson, *Electrochem. Commun.* **2022**, *139*, 107304.
[33] A. J. Merryweather, C. Schnedermann, Q. Jacquet, C. P. Grey, A. Rao, *Nature.* **2021**, *594*, 522.
[34] A. J. Merryweather, Q. Jacquet, S. P. Emge, C. Schnedermann, A. Rao, C. P. Grey, *Nat. Mater.* **2022**, *21*, 1306.
[35] C. Xu, A. J. Merryweather, S. S. Pandurangi, Z. Lun, D. S. Hall, V. S. Deshpande, N. A. Fleck, C. Schnedermann, A. Rao, C. P. Grey, *Joule.* **2022**, *6*, 2535.
[36] S. Redor, L. Godeffroy, G. Rousse, A. M. Abakumov, B. Li, F. Kanoufi, J.-M. Tarascon, *J. Am. Chem. Soc.* **2023**, *145*, 12823.
[37] R. Pandya, L. Valzania, F. Dorchies, F. Xia, J. Mc Hugh, A. Mathieson, H. J. Tan, T. G. Parton, L. Godeffroy, K. Mazloomian, T. S. Miller, F. Kanoufi, M. De Volder, J.-M. Tarascon, S. Gigan, H. B. de Aguiar, A. Grimaud, *Nat. Nanotechnol.* **2023**, *18*, 1185.
[38] W. Wei, T. Yuan, W. Jiang, J. Gao, H.-Y. Chen, W. Wang, *J. Am. Chem. Soc.* **2020**, *142*, 14307.
[39] T. Yuan, W. Wei, W. Jiang, W. Wang, *ACS Nano.* **2021**, *15*, 3522.
[40] B. Niu, W. Jiang, B. Jiang, M. Lv, S. Wang, W. Wang, *Nat. Commun.* **2022**, *13*, 2316.
[41] R. C. Evans, Z. N. Nilsson, J. B. Sambur, *Anal. Chem.* **2019**, *91*, 14983.
[42] R. C. Evans, A. Ellingworth, C. J. Cashen, C. R. Weinberger, J. B. Sambur, *Proc. Natl. Acad. Sci* **2019**, *116*, 12666.
[43] W. Jiang, W. Wei, T. Yuan, S. Liu, B. Niu, H. Wang, W. Wang, *Chem. Sci.* **2021**, *12*, 8556.
[44] K. O. Hatfield, M. T. Gole, N. B. Schorr, C. J. Murphy, J. Rodríguez-López, *Anal. Chem.* **2021**, *93*, 7792.
[45] N. B. Schorr, A. G. Jiang, J. Rodríguez-López, *Anal. Chem.* **2018**, *90*, 7848.
[46] J. Clausmeyer, M. Nebel, S. Grützke, Y. U. Kayran, W. Schuhmann, *ChemPlusChem.* **2018**, *83*, 414.
[47] L. Wang, J. Kowalik, B. Mizaikoff, C. Kranz, *Anal. Chem.* **2010**, *82*, 3139.
[48] M. Etienne, M. Dossot, J. Grausem, G. Herzog, *Anal. Chem.* **2014**, *86*, 11203.
[49] L. Guerret-Legras, J. F. Audibert, G. V. Dubacheva, F. Miomandre, *Chem. Sci.* **2018**, *9*, 5897.
[50] F.-M. Boldt, J. Heinze, M. Diez, J. Petersen, M. Börsch, *Anal. Chem.* **2004**, *76*, 3473.
[51] D. Valavanis, P. Ciocci, G. N. Meloni, P. Morris, J. Lemineur, I. J. McPherson, F. Kanoufi, P. R. Unwin, *Faraday Discuss.* **2022**, *233*, 122.
[52] L. Godeffroy, J.-F. Lemineur, V. Shkirskiy, M. Miranda Vieira, J.-M. Noël, F. Kanoufi, *Small Methods.* **2022**, *6*, 2200659.
[53] M. M. Rahman, C. L. Tolbert, P. Saha, J. M. Halpern, C. M. Hill, *ACS Nano.* **2022**, *16*, 21275.
[54] D. O. Ojwang, J. Grins, D. Wardecki, M. Valvo, V. Renman, L. Häggström, T. Ericsson, T. Gustafsson, A. Mahmoud, R. P. Hermann, G. Svensson, *Inorg. Chem.* **2016**, *55*, 5924.
[55] P. Hosseini, K. Wolkersdörfer, M. Wark, E. Redel, H. Baumgart, G. Wittstock, *J. Phys. Chem. C.* **2020**, *124*, 16849.
[56] F. Kanoufi, *Encyclopedia of Electrochemistry*, Wiley, Weinheim, Germany **2021**, https://doi.org/10.1002/9783527610426.bard030108.
[57] A. P. Baioni, M. Vidotti, P. A. Fiorito, E. A. Ponzio, S. I. Córdoba de Torresi, *Langmuir.* **2007**, *23*, 6796.
[58] E. S. Goda, S. Lee, M. Sohail, K. R. Yoon, *J. Energy Chem.* **2020**, *50*, 206.
[59] A. I. Komayko, N. A. Arkharova, D. E. Presnov, E. E. Levin, V. A. Nikitina, *J. Phys. Chem. Lett.* **2022**, *13*, 3165.
[60] M. Guo, R. E. White, *J. Power Sources.* **2012**, *198*, 322.